SMA-based adaptive tuned mass dampers: Analysis and comparison

SMA-based adaptive tuned mass dampers: analysis and comparison

S. Manzoni[1], A. Argentino[1], F. Lucà[1], M. Berardengo[2], M. Vanali[3]

1. Politecnico di Milano – Department of Mechanical Engineering
Via La Masa, 1 – 20156 Milan, Italy
2. Università degli Studi di Genova - Department of Mechanical, Energy, Management and Transportation Engineering
Via all'Opera Pia, 15A - 16145 Genoa, Italy
3. Università degli Studi di Parma - Department of Engineering and Architecture
Parco Area delle Scienze, 181/A – 43124 Parma, Italy

Abstract

Different types of adaptive tuned mass dampers have been recently proposed in the literature. One of the most promising approaches to make tuned mass dampers adaptive is the use of shape memory alloys. In this class of tuned mass dampers, different layouts have been proposed. This paper aims at comparing the two main layouts (wire-based and beam-based) in terms of adaptation capability, exerted force and electrical power consumption. To this purpose, the models of the two layouts are developed. These models minimise the number of required inputs, which basically are only related to device geometry, shape memory alloy characteristics, and vibration input. After an experimental validation, the models are employed for the mentioned comparisons between the two considered layouts.

Key words: `tuned mass damper, adaptive tuned mass damper, shape memory alloy, vibration, damping`

*stefano.manzoni@polimi.it
Email address: (S. Manzoni[1], A. Argentino[1], F. Lucà[1], M. Berardengo[2], M. Vanali[3])

1. Introduction

The use of tuned mass dampers (TMDs) is widely accepted for attenuating vibrations of a primary structure (PS). The basic principle that allows for a proper functioning of the TMD is that its eigenfrequency must be tuned close to the eigenfrequency of the PS to be attenuated, e.g., [1, 2].

The main issue related to these devices is that, when a mistuning between the TMD and the PS eigenfrequencies occurs (e.g., due to thermal shifts causing changes of the eigenfrequencies), the effectiveness of the control action worsens. To solve such a problem, adaptive tuned mass dampers (ATMDs) can be built. These devices are able to change their dynamic features and, particularly, they can change their eigenfrequency (e.g., [3]) to follow the change of the PS eigenfrequency. Different methods and physical principles can be employed to build ATMDs. As examples, the use of servo-actuators (e.g., [4]), piezoelectric (e.g., [5–7]) and magnetorheological (e.g., [8, 9]) elements, tensioning systems [10] and pneumatic springs (e.g., [11]) can be mentioned. A very promising approach for attenuating vibrations, and more specifically for developing ATMDs, is the use of shape memory alloys (SMAs) (e.g., [12–14]), whose features are suitable for easily changing the TMD eigenfrequency. This change can be obtained exploiting different properties of the SMAs and this allows for different layouts of the ATMD. Nevertheless, in all the possible layouts, the change of the dynamic features of the ATMD is obtained by heating/cooling the SMA element by increasing/decreasing the current flowing through the SMA element itself.

The two main layouts discussed in the literature are SMA cantilever beams [15–17] and SMA wires [18–20], even if other layouts are possible (e.g., [21–23]). Even if both cantilever beams and wires showed to provide good vibration attenuation capabilities, no detailed comparisons are available between the two of them. This paper aims at filling this gap, comparing the two layouts under different points of views. Particularly, the following aspects will be addressed in this work:

- adaptation capability which indicates how much the ATMD eigenfrequency can be changed. It is noticed that, for damping adaptation, both the ATMD layouts can be easily coupled to similar additional devices such as, e.g., eddy current devices [18];

- force exerted by the ATMD on the PS, which is related to the attenuation performance that can be achieved;

- power consumption related to the need of having electrical current flowing through the SMA elements.

The mentioned comparisons are made possible by developing detailed models of the two types of ATMDs. Compared to models already available in the literature, those proposed here minimise the number of inputs, which will result in the need of knowing only geometrical and material characteristics, as well as the vibration input. Particularly, it will be shown how to estimate, through models, quantities involved in the thermal exchange with the environment, which are usually characterised by significant uncertainty when directly estimated experimentally. The developed global models will allow for directly linking the input quantity (i.e., electrical current flowing through the SMA element, as explained further in the manuscript) to the dynamic behaviour of the ATMD.

The structure of the paper is as follows: Section 2 recalls the main features of the SMA elements and presents the two ATMD layouts considered here, Section 3 presents the models of the two ATMD types and Section 4 discusses the experimental validation of the proposed models. Then, Section 5 addresses the comparisons between the two types of ATMDs using these models.

2. SMA features and ATMD layouts

This section aims at explaining which SMA features are exploited to develop the two different ATMD layouts. Figure 1 presents the typical stress-temperature plot of SMA materials [24], where the three possible phases of

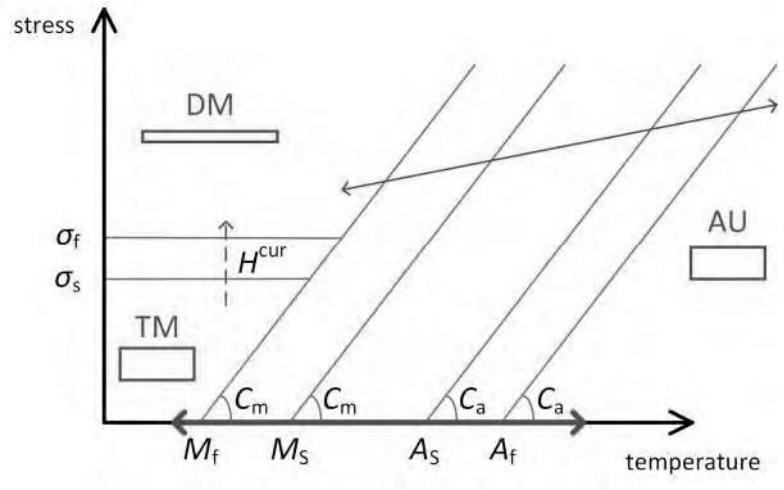

Figure 1: Principles of SMA phase transformations used in this paper.

the material are evidenced: austenite (AU), twinned martensite (TM) and detwinned martensite (DM). The symbols in the figure represent the following quantities: σ_s and σ_f are the stress values at which the transformation from TM to DM starts and ends, respectively, at the environmental temperature T_0, while A_s and A_f are the temperature values at which the transformation from TM to AU starts and ends, respectively, at null stress. M_s and M_f have the same meaning of A_s and A_f, but for the transformation from AU to TM. Finally, C_a and C_m are the angular coefficients of the transformation lines and H^{cur} is the strain due to the change of shape during the phase transition between TM and DM (see the vertical red dashed arrow in Figure 1), named the current maximum transformation strain. More details about this plot can be found in, e.g., [18, 19, 24].

It is possible to pass from TM and AU and vice versa by changing the temperature at null stress (see the thick red solid double arrow in Figure 1). Since the SMA material has the same shape in AU and TM, the main change in the SMA element during the mentioned transformation is related to the Young's modulus. This principle is used to build SMA cantilever beams, whose eigenfrequency is changed by changing the temperature of the beam. The change

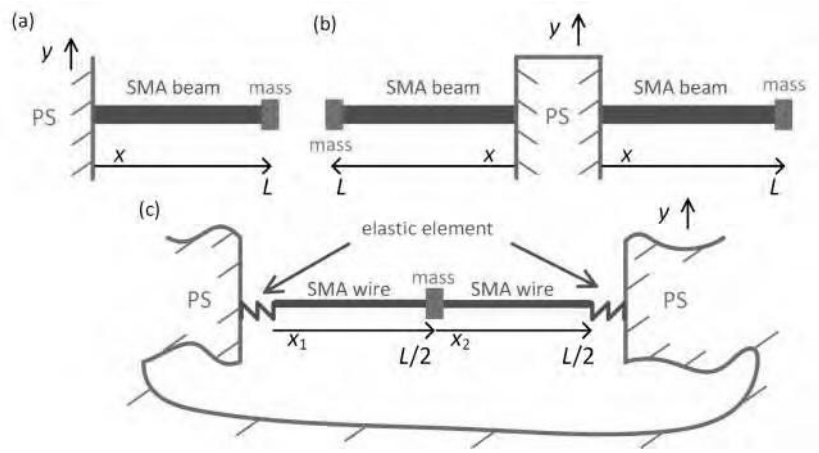

Figure 2: Layouts of ATMDs: single cantilever beam (a), double cantilever beam (b) and wire with central mass (c).

of temperature is achieved by changing the value of the electrical current flowing through the beam. A single cantilever beam exerts a force and a torque on the PS (see Figure 2a). Therefore, in this paper, a configuration with a double cantilever beam is considered in order to have only a linear force, avoiding the torque (see Figure 2b).

Another way to have a phase transformation in the SMA material is to apply a stress over σ_f and then change temperature to pass from DM to AU and vice versa, as evidenced by the thin red solid double arrow in Figure 1. This double arrow does not mean that the temperature-stress states experienced by the SMA element are the same in both the directions of transformation, but only that, changing temperature, also a change of stress occurs. In this case, the eigenfrequency change is mainly related to the change of shape (between AU and DM), even if also a change of the material parameters occurs [18]. Relying on this principle, it possible to build an ATMD by means of an oscillating SMA wire with a central mass. The SMA wire is pre-stressed over σ_f by employing elastic elements which also connect the SMA wire to the PS (see Figure 2c). Also in this case, the change of temperature is achieved by changing the value of the electrical current that is made flow through the SMA wire.

Finally, it is noticed that the treatment used here always considers small amplitude vibrations (e.g., those obtained when random excitation is considered) and, thus, stress-induced phase transformations (e.g., [25]) are neglected here. Nevertheless, the models described in this paper can be considered as a starting point for more complicated ones accounting also for the case of large amplitude vibrations.

3. Analytical models of the ATMDs

The model of the ATMD must describe the relationship between the input parameter, which is the current made flow through the SMA component, and the dynamics of the ATMD, with special focus on the value of its first eigenfrequency and the frequency response function (FRF) between the imposed motion $y(t)$ (see Figure 2, t is time) and the force exerted on the PS by the ATMD.

To obtain this global model, different aspects must be addressed, from the thermal effects to the dynamics of the vibrating structure. For this reason, the global model is split as the sequence of three different submodels: a thermal model, a material model and a dynamic model. Subsections 3.1 to 3.3 will treat in detail the three submodels, while subsection 3.4 will explain how to link them to obtain the final global model. In each of these subsections, both the types of ATMDs discussed previously will be considered. It is noticed that parts of the models discussed here were already developed in previous works (e.g., [18, 24]). Nevertheless, some parts of the models presented in the following subsections either are new or have been further developed in order to minimise the number of inputs required to estimate the ATMD dynamics. As an example, the convective coefficient (see Section 3.1) is now directly derived through the model by only measuring $y(t)$, avoiding to experimentally estimate quantities whose measurements are affected by significant uncertainty.

3.1. Thermal model

This submodel aims at describing how to link the input current i flowing through the SMA element to the achieved temperature. Considering at first to

have a cylindrical shape for the SMA element, the power balance in steady state can be written as:

$$A_{\text{ext}} h (T - T_0) = R i^2 \tag{1}$$

where T, R and A_{ext} are the temperature, the resistance and the outer area of the SMA element, respectively. Finally, h is the convective heat transfer coefficient. It is noticed that the left-hand term of Eq. (1) is related to the energy output, while the right-hand term to the energy input (i.e., Joule's effect). Furthermore, being D the external diameter of the SMA element and L_{tot} its global length (i.e., $L_{\text{tot}} = 2L$ for the beam-based ATMD, see Fig. 2b, and $L_{\text{tot}} = L$ for the wire-based ATMD, see Fig. 2c, considering the wires/beams electrically connected in series), A_{ext} can be expressed as $\pi D L_{\text{tot}}$. Obviously, in case the SMA element is a hollow cylinder, A_{ext} would be equal to $\pi(D+d)L_{\text{tot}}$ (being d the internal diameter). Nevertheless, since D is higher than d and the internal outer surface is expected to have less heat exchange with the air compared to the outer external surface of the cylinder (due to, e.g., less relevant air flux inside than outside), here A_{ext} will be always considered equal to $\pi D L_{\text{tot}}$ even in case of hollow cylinder.

To calculate T by means of Eq. (1) once i has been fixed, h and R must be determined. Concerning R, it can be calculated as:

$$R = \rho L_{\text{tot}} / A \tag{2}$$

where A is the cross-section of the SMA element and ρ is its resistivity. Therefore, to obtain the value of R, the value of ρ must be estimated. The trend of the resistivity depends on the entire history of the specific SMA element, from the processing technology to the heat treatments. Therefore, to simplify the model in order to make it easy enough to be applied in practice, a linear variation of ρ between austenite and martensite is used here. This assumption is reasonable for the sake of the paper aim and it is often employed also for other material parameters (e.g., for the Young's modulus [24], see also Section

3.2) for mono-dimensional elements like beams and wires. Thus, the expression of ρ becomes:

$$\rho = \rho_{\mathrm{a}} + \xi(\rho_{\mathrm{m}} - \rho_{\mathrm{a}}) \tag{3}$$

where the subscripts 'a' and 'm' indicate austenite and martensite, respectively. Moreover, ξ is the martensite volume fraction (i.e., ξ=0 when the material is fully austenitic, and ξ=1 when it is fully martensitic).

Therefore, to estimate the value of ρ while heating/cooling the SMA element, it is only necessary to know ρ_{a} and ρ_{m}, whose values can be estimated through experiments, and ξ which can be deduced from the material model (see Section 3.2).

The other parameter that must be estimated in order to find T using Eq. (1) is h. To derive the h value, the following procedure is employed. Considering the SMA element as a cylinder (see previously) vibrating in air, the Nusselt number N_{u} can be defined as:

$$N_{\mathrm{u}} = \frac{hD}{\psi_{\mathrm{A}}} \tag{4}$$

where ψ_{A} is the thermal conductivity of air. Therefore, h can be estimated by means of Eq. (4) and knowing in advance the value of the Nusselt number. Considering a forced external cross flow over a cylinder, N_{u} can be estimated as [26]:

$$N_{\mathrm{u}} = 0.3 + \frac{0.62 R_{\mathrm{e}}^{(1/2)} P_{\mathrm{r}}^{(1/3)}}{[1 + (\frac{0.4}{P_{\mathrm{r}}})^{(2/3)}]^{(1/4)}} [1 + (R_{\mathrm{e}}/282000)^{(5/8)}]^{(4/5)} \tag{5}$$

where R_{e} and P_{r} are the Reynolds and Prandtl numbers, respectively. Their expressions are:

$$R_{\mathrm{e}} = \frac{r_{\mathrm{A}} v_{\mathrm{c}} D}{b_{\mathrm{A}}} \tag{6}$$

$$P_{\mathrm{r}} = \frac{\eta_{\mathrm{A}} b_{\mathrm{A}}}{\psi_{\mathrm{A}}} \tag{7}$$

where r_A is the density of the air, b_A is its dynamic viscosity and η_A is its specific heat. Finally, v_c is an index expressing the velocity of the cylinder (in vertical direction that is the velocity related to vibration, see Fig. 2). Equations (4) to (7) allow calculating h once v_c is known. One must consider that the velocity of the beam/wire is a function of time t and space (for beams and wires, it means that the velocity is a function of the coordinates x, x_1 and x_2 along the elements, refer to Fig. 2). Thus, a synthetic expression must be found for v_c. The velocity v of each point of the beam/wire can be expressed as:

$$\begin{aligned} v(x,t,T) = \frac{\partial w(x,t,T)}{\partial t} &= \frac{\partial\left[\mathrm{F}^{-1}\{G_{\mathrm{WY}}(x,\mathrm{j}\Omega,T)\}\otimes y(t)\right]}{\partial t} \\ &= \mathrm{F}^{-1}\{\mathrm{j}\Omega G_{\mathrm{WY}}(x,\mathrm{j}\Omega,T)Y(\mathrm{j}\Omega)\} \end{aligned} \tag{8}$$

where $w(x,t,T)$ is the vertical displacement of the beam/wire as function of x (see Figs. 2b and c), t, and T, $\otimes$ indicates the convolution operation, $\mathrm{F}^{-1}\{\cdot\}$ is the inverse Fourier transform of a complex quantity, y is the displacement of the PS (see Fig. 2), Ω is the angular frequency, j is the imaginary unit and G_{WY} is the following FRF:

$$G_{\mathrm{WY}}(x,\mathrm{j}\Omega,T) = \frac{W(x,\mathrm{j}\Omega,T)}{Y(\mathrm{j}\Omega)} \tag{9}$$

where Y and W are the Fourier transform of y and w, respectively. The way to derive $G_{\mathrm{WY}}(x,\mathrm{j}\Omega,T)$ is discussed in Section 3.3. At first, the average-rectified value of v, named v_r, is calculated on the considered time interval 0-t_f. For the case of the two beams, for each of them v_r is:

$$v_r(x,T) = \frac{1}{t_f}\int_0^{t_f} |v(x,t,T)|\,\mathrm{d}t \tag{10}$$

For the case of the wire, v_r is:

$$v_r(x_1,T) = \frac{1}{t_f}\int_0^{t_f} |v(x_1,t,T)|\,\mathrm{d}t, \quad v_r(x_2,T) = \frac{1}{t_f}\int_0^{t_f} |v(x_2,t,T)|\,\mathrm{d}t \tag{11}$$

Then, v_c is obtained averaging v_r over the length of the SMA element. For the double beam and thanks to the system symmetry (i.e., assuming the same motion for the two beams, see Section 3.3.1), it is:

$$v_{\mathrm{c}}(T) = \frac{1}{L}\int_0^L v_{\mathrm{r}}(x,T)\,\mathrm{d}x \tag{12}$$

For the case of the wire, it is:

$$v_{\mathrm{c}}(T) = \frac{1}{L}\left[\int_0^{L/2} v_{\mathrm{r}}(x_1,T)\,\mathrm{d}x_1 + \int_0^{L/2} v_{\mathrm{r}}(x_2,T)\,\mathrm{d}x_2\right] \tag{13}$$

It is noticed that $y(t)$ must be estimated/measured to derive v_{c} (see Eq. (8)).

3.2. Model of the material

The material model is here based on the Experimentally-Based 1-D Material Model [24], where the following assumptions are considered:

- the Young's modulus E of the SMA material is linearly dependent on ξ:

$$E = E_{\mathrm{a}} + \xi(E_{\mathrm{m}} - E_{\mathrm{a}}) \tag{14}$$

- the thermal expansion coefficient α is constant
- the 1-D transformation strain ε^{t} is linearly dependent on ξ:

$$\varepsilon^{\mathrm{t}} = \xi H^{\mathrm{cur}} \tag{15}$$

  It is noticed that Eq. (15) is related to cases in which the SMA element is stressed and the phase transformation between TM and DM is triggered. When this does not occur and only transformations between TM and AU and vice versa are considered, ε^{t} is null.

- the starting and ending transformation temperatures (i.e., M_{s}^{σ}, M_{f}^{σ}, A_{s}^{σ}, A_{f}^{σ}) are linearly dependent on the stress σ into the SMA element (see Fig. 1):

$$M_{\mathrm{s}}^{\sigma} = M_{\mathrm{s}} + \frac{\sigma}{C_{\mathrm{m}}},\quad M_{\mathrm{f}}^{\sigma} = M_{\mathrm{f}} + \frac{\sigma}{C_{\mathrm{m}}},\quad A_{\mathrm{s}}^{\sigma} = A_{\mathrm{s}} + \frac{\sigma}{C_{\mathrm{a}}},\quad A_{\mathrm{f}}^{\sigma} = A_{\mathrm{f}} + \frac{\sigma}{C_{\mathrm{a}}} \tag{16}$$

- the value of ξ during transformation from martensite to AU (i.e., either increase of temperature T or decrease of stress σ, see Fig. 1) is described as:

$$\begin{cases} 1, & T \leq A_{\mathrm{s}}^{\sigma} \\ \frac{A_{\mathrm{f}}^{\sigma}-T}{A_{\mathrm{f}}-A_{\mathrm{s}}}, & A_{\mathrm{s}}^{\sigma} < T < A_{\mathrm{f}}^{\sigma} \\ 0, & T \geq A_{\mathrm{f}}^{\sigma} \end{cases} \tag{17}$$

  while during transformation from AU to martensite (i.e., either decrease of temperature T or increase of stress σ) it is assumed as:

$$\begin{cases} 0, & T \geq M_{\mathrm{s}}^{\sigma} \\ \frac{M_{\mathrm{s}}^{\sigma}-T}{M_{\mathrm{s}}-M_{\mathrm{f}}}, & M_{\mathrm{f}}^{\sigma} < T < M_{\mathrm{s}}^{\sigma} \\ 1, & T \leq M_{\mathrm{f}}^{\sigma} \end{cases} \tag{18}$$

  It is noticed that Eqs. (17) and (18) are valid for transformations starting from homogeneous material (i.e., either ξ=1 or ξ=0). When transformations starting from a non-homogeneous material (i.e., 0< ξ <1) are considered, these equations can be slightly complicated in order to address also these additional cases, making the equations general. These general expressions can be found in the literature (see, e.g., [18, 19] for more details), but they are neglected here for the sake of conciseness and because they are not the focus of this paper.

When an ATMD based on an SMA beam is considered, σ is assumed to be null, because no external stress is applied and that caused by vibrations is assumed to be small enough for being neglected, and ε^{t} is null as well. Therefore, using the previous equations, one can estimate the value of E once the temperature T is known thanks to the thermal model of Section 3.1. Moreover, the influence of T on the length L is assumed negligible here (i.e., L is constant).

When an ATMD based on an SMA wire is considered, the analytical treatment becomes more complicated because σ is not null due to the elastic elements

(see Fig. 2c). In this case, the global strain ε of the wire is:

$$\varepsilon = \varepsilon^{\mathrm{t}} + \varepsilon^{\mathrm{e}} + \varepsilon^{\mathrm{th}} = \frac{\Delta L}{L\mathrm{unst}} \tag{19}$$

where ε^{e} and $\varepsilon^{\mathrm{th}}$ are the elastic strain and the thermal strain (i.e., due to thermal expansion), respectively. Finally, ΔL indicates a change of L and L_{unst} is the length of the non-strained SMA wire.

When the value of T passes from T_{ini} to T_{fin}, the following equation can be written (noticing that an increase of temperature generates a shortening of the wire, which passes from DM to AU, and vice versa):

$$\begin{gathered}\Delta\varepsilon = \varepsilon_{\mathrm{fin}} - \varepsilon_{\mathrm{ini}} = \frac{L_{\mathrm{fin}}/2 - L_{\mathrm{ini}}/2}{L_{\mathrm{unst}}/2} = \frac{-(F_{\mathrm{fin}} - F_{\mathrm{ini}})}{KL_{\mathrm{unst}}/2} = \\ (\frac{\sigma_{\mathrm{fin}}}{E_{\mathrm{fin}}} - \frac{\sigma_{\mathrm{ini}}}{E_{\mathrm{ini}}}) + [\alpha(T_{\mathrm{fin}} - T_{\mathrm{ini}})] + (\xi_{\mathrm{fin}} - \xi_{\mathrm{ini}})H^{\mathrm{cur}}\end{gathered} \tag{20}$$

where K indicates the elastic constant of each spring in Fig. 2c, while F is the axial force in the wire (F is positive when tensioning the wire, see also [18]).

All the variables at the new state "fin" in Eq. (20) are dependent on T_{fin} and σ_{fin} through the equations presented in this subsection. Therefore, knowing the previous situation of the ATMD at state "ini", and estimating T_{fin} with the thermal model of Section 3.1 (see Section 3.4.2 for more details), it is possible to calculate σ_{fin}. Then, also F_{fin} (i.e., $F_{\mathrm{fin}} = \sigma_{\mathrm{fin}}/A$) and L_{fin} (see Eq. (20)) can be calculated.

3.3. Dynamic model

This section presents the dynamic model for the beam (Section 3.3.1) and the wire (Section 3.3.2).

3.3.1. Vibrating beam

At first, a single cantilever beam is considered (see Fig. 2a) and then the results are extended to the double cantilever beam (see Fig. 2b). The dynamic model of the vibrating beam is developed under the following hypotheses:

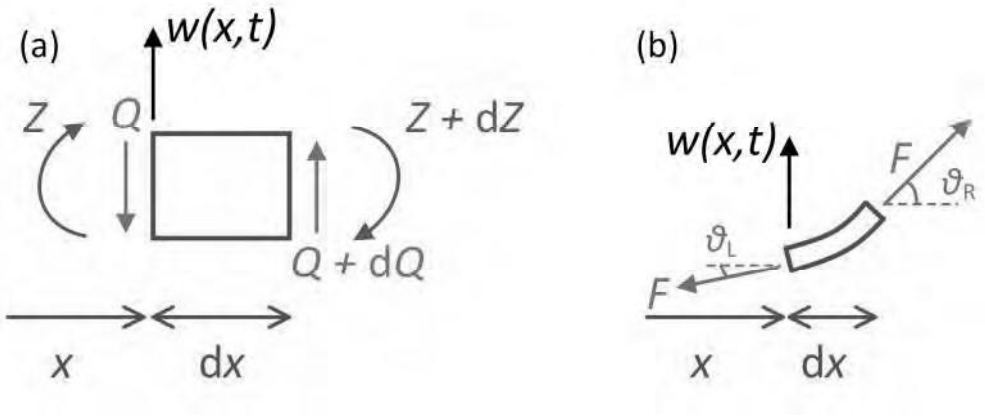

Figure 3: Forces and torques acting on the infinitesimal portion of beam (a) and wire (b).

- the beam is homogeneous, with constant bending stiffness EJ (where J is the cross-section moment of inertia), cross-section A and mass per unit length μ (with $\mu = \theta_{\mathrm{m}} A$, being θ_{m} the mass density);
- the beam is slender (i.e., its length is much greater than the dimensions of the cross-section);
- the sections perpendicular to the axis remain plane;
- even under dynamic conditions, the beam undergoes always to bending in a plane of symmetry;
- the amplitude of vibration is small enough to assume non-linearity as negligible;
- axial load is absent;
- damping is neglected.

Under these hypotheses, the equation of motion of the beam is [27, 28]:

$$EJ \frac{\partial^4 w(x,t)}{\partial x^4} + \theta_{\mathrm{m}} A \frac{\partial^2 w(x,t)}{\partial t^2} = 0 \tag{21}$$

Equation (21), that results from the equilibria of force and momentum on an infinitesimal beam element of length dx (see Fig. 3a for the convention of sign, where Z and Q are the internal actions), can be written as a function of the relative displacement $w_{\mathrm{rel}}(x,t) = w(x,t) - y(t)$ (thus, in a frame moving with the PS):

$$EJ\frac{\partial^4 w_{\mathrm{rel}}(x,t)}{\partial x^4} + \theta_{\mathrm{m}} A \frac{\partial^2 w_{\mathrm{rel}}(x,t)}{\partial t^2} = -\theta_{\mathrm{m}} A \frac{\mathrm{d}^2 y(t)}{\mathrm{d}t^2} \tag{22}$$

It is noticed that the term in the right-hand side of Eq. (22), due to the inertia of the beam, is related to an external distributed force (constant along the beam) acting on the beam. In order to derive the eigenfrequencies and mode shapes, the free vibrations of the beam have to be studied and, thus, this forcing term is neglected. The solution of this problem is provided in Appendix A and the FRF between Y and W results equal to:

$$G_{\mathrm{WY}}(x,\mathrm{j}\Omega) = \frac{W(x,\mathrm{j}\Omega)}{Y(\mathrm{j}\Omega)} = 1 + \sum_{i=1}^{n} \frac{\Omega^2 \phi_i(x)\left[\theta_{\mathrm{m}} A \int_0^L \phi_i(x)\mathrm{d}x + M_{\mathrm{a}}\phi_i(L)\right]}{m_i(-\Omega^2 + 2\mathrm{j}\zeta_i\omega_i\Omega + \omega_i^2)} \tag{23}$$

where ζ_i is the non-dimensional damping ratio associated to the i-th eigenfrequency ω_i (proportional damping is added in the mathematical treatment in Appendix A); moreover, $\phi_i(x)$ and m_i are the i-th mode shape and modal mass, respectivley. Finally, M_{a} is the value of the additional mass at the beam tip (see Fig. 2a) and n is the number of modes. Furthermore, the FRF between $Y(\mathrm{j}\Omega)$ and the vertical force exerted on the PS $S(\mathrm{j}\Omega)$ ($S(\mathrm{j}\Omega)$ is the Fourier transform of the force $s(t)$ exerted by the ATMD on the PS, see Appendix A) can also be found and results equal to:

$$G_{\mathrm{SY}}(\mathrm{j}\Omega) = \frac{S(\mathrm{j}\Omega)}{Y(\mathrm{j}\Omega)} = -2EJ \sum_{i=1}^{n} \frac{\Omega^2 \phi_i'''(0)\left[\theta_{\mathrm{m}} A \int_0^L \phi_i(x)\mathrm{d}x + M_{\mathrm{a}}\phi_i(L)\right]}{m_i(-\Omega^2 + 2\mathrm{j}\zeta_i\omega_i\Omega + \omega_i^2)} \tag{24}$$

with

$$\phi_i'''(0) = \left.\frac{\mathrm{d}^3\phi_i(x)}{\mathrm{d}x^3}\right|_{x=0} \tag{25}$$

It is noticed that Eq. (24) accounts for the presence of two SMA beams as in Fig. 2b.

3.3.2. Vibrating wire

The dynamic model of the vibrating wire is developed under the following hypotheses:

- the mass density θ_{m} and the cross-section A of the strings are constant along the length of the strings;
- the shear force and bending moment are neglected;
- the amplitude of vibration is small enough to assume non-linearity as negligible;
- the axial force F into the wire is high compared to the static load of the central mass, so that the wire configuration in equilibrium can be approximated as rectilinear;
- the central mass is a concentrated mass;
- damping is neglected.

Under these hypotheses, the equation of motion of the wire is [19, 27–29]:

$$F\frac{\partial^2 w(x,t)}{\partial x^2} = \theta_{\mathrm{m}} A \frac{\partial^2 w(x,t)}{\partial t^2} \tag{26}$$

Equation (26), that results from the equilibrium of vertical force on an infinitesimal element of length $\mathrm{d}x$ (see Fig. 3b for the convention of sign), can be written as a function of the relative displacement $w_{\mathrm{rel}}(x,t) = w(x,t) - y(t)$ (thus, in a frame moving with the PS):

$$F\frac{\partial^2 w_{\mathrm{rel}}(x,t)}{\partial x^2} - \theta_{\mathrm{m}} A \frac{\mathrm{d}^2 y(t)}{\mathrm{d}t^2} = \theta_{\mathrm{m}} A \frac{\partial^2 w_{\mathrm{rel}}(x,t)}{\partial t^2} \tag{27}$$

Equation (27) is valid for both the wires, i.e. that between the left constraint and the central mass, and that between the central mass and the right constraint

(see Fig. 2c). The solution of the dynamic problem for each of the wires can be found (e.g. [27, 28]) and it is provided in Appendix B.

The FRF between Y and W for the first wire is (introducing proportional damping in the mathematical treatment, see Appendix B):

$$G_{\mathrm{WY}}(x_1,\mathrm{j}\Omega)=\frac{W(x_1,\mathrm{j}\Omega)}{Y(\mathrm{j}\Omega)}= \\ 1+\sum_{i=1}^{n}\frac{\Omega^2\phi_{i,1}(x_1)\left[\theta_{\mathrm{m}}A(\int_0^{L/2}\phi_{i,1}(x_1)\mathrm{d}x_1+\int_0^{L/2}\phi_{i,2}(x_2)\mathrm{d}x_2)+M_{\mathrm{a}}\phi_{i,1}(L/2)\right]}{m_i(-\Omega^2+2\mathrm{j}\zeta_i\omega_i\Omega+\omega_i^2)} \tag{28}$$

and for the second wire is:

$$G_{\mathrm{WY}}(x_2,\mathrm{j}\Omega)=\frac{W(x_2,\mathrm{j}\Omega)}{Y(\mathrm{j}\Omega)}= \\ 1+\sum_{i=1}^{n}\frac{\Omega^2\phi_{i,2}(x_2)\left[\theta_{\mathrm{m}}A(\int_0^{L/2}\phi_{i,1}(x_1)\mathrm{d}x+\int_0^{L/2}\phi_{i,2}(x_2)\mathrm{d}x_2)+M_{\mathrm{a}}\phi_{i,2}(0)\right]}{m_i(-\Omega^2+2\mathrm{j}\zeta_i\omega_i\Omega+\omega_i^2)} \tag{29}$$

The FRF between $Y(\mathrm{j}\Omega)$ and the vertical force exerted on the PS $S(\mathrm{j}\Omega)$ ($S(\mathrm{j}\Omega)$ is the Fourier transform of $s(t)$, see Appendix B) is

$$G_{\mathrm{SY}}(\mathrm{j}\Omega)=\frac{S(\mathrm{j}\Omega)}{Y(\mathrm{j}\Omega)}= \\ F\Omega^2\sum_{i=1}^{n}\left\{\left[\phi_{i,1}^{'}(0)-\phi_{i,2}^{'}(L/2)\right]\frac{\left[\theta_{\mathrm{m}}A(\int_0^{L/2}\phi_{i,1}(x_1)\mathrm{d}x_1+\int_0^{L/2}\phi_{i,2}(x_2)\mathrm{d}x_2)+M_{\mathrm{a}}\phi_{i,1}(L/2)\right]}{m_i(-\Omega^2+2\mathrm{j}\zeta_i\omega_i\Omega+\omega_i^2)}\right\} \tag{30}$$

with:

$$\phi_{i,1}^{'}(0)=\left.\frac{\mathrm{d}\phi_{i,1}(x_1)}{\mathrm{d}x_1}\right|_{x_1=0},\quad \phi_{i,2}^{'}(L/2)=\left.\frac{\mathrm{d}\phi_{i,2}(x_2)}{\mathrm{d}x_2}\right|_{x_2=L/2} \tag{31}$$

It is noticed that, for the first eigenmode, that is the interesting one in this case, $\phi_{i,1}^{'}(0)-\phi_{i,2}^{'}(L/2)$ reduces to $2\phi_{i,1}^{'}(0)$ because of the symmetry of the mode and the system.

3.4. Global model

The three submodels described so far are now assembled in order to derive a general model which enables estimating the ATMD FRFs G_{WY} and G_{SY} once i is set by the user. Subsections 3.4.1 and 3.4.2 describe the global model for the case of the beam and the wire, respectively.

Table 1: Input data for the global model.

Beam	Wire
M_s, M_f, A_s, A_f, $\zeta_{i,\mathrm{a}}$, $\zeta_{i,\mathrm{m}}$, ρ_a, ρ_m,	M_s, M_f, A_s, A_f, C_m, C_a, H^cur, K, E_ini, T_ini,
E_a, E_m, J, M_a, L, θ_m, A, D, d,	σ_ini, ξ_ini, $\zeta_{i,\mathrm{a}}$, $\zeta_{i,\mathrm{m}}$, ρ_a, ρ_m, E_a, E_m, J, M_a,
A_ext, T_0, ψ_A, r_A, b_A, η_A, $y(t)$	L_unst, θ_m, A, D, A_ext, T_0, ψ_A, r_A, b_A, η_A, $y(t)$

3.4.1. Global model for the beam

The input parameters of the global model, which have to be either estimated/known in advance or measured are gathered in Table 1. At first, Eqs. (17) and (18) are used to find the link between T and ξ for the two types of transformation and the considered T values (when using these equations, L is considered as constant and the stress into the beam as null; see Section 3.2). Then, Eqs. (3) and (14) are employed to estimate ρ and E, respectively, for each considered T value and type of transformation. Then the FRFs of Eqs. (23) and (24) can be estimated. This procedure allows to find two FRFs for each T value in each transformation. These FRFs are then used to estimate h through Eqs. (4) to (12). The knowledge of h then allows for finding the relationship between i and T by means of Eq. (1) for the two transformations. The knowledge of these relationships enables estimating the beam temperature and its FRFs when a given value of i is set by the user.

One further notation is worth being mentioned. In Eqs. (23) and (24), ζ_i must be calculated for all the possible values of i and T. This is a complicated task and, according to previous considerations, in this work the following approximation is adopted:

$$\zeta_i = \zeta_{i,\mathrm{a}} + \xi(\zeta_{i,\mathrm{m}} - \zeta_{i,\mathrm{a}}) \tag{32}$$

3.4.2. Global model for the wire

The input parameters of the global model, which have to be either estimated/known in advance or measured are presented in Table 1. At first, Eqs. (17) and (18) are used in Eq. (20) to find the link between T and σ for the two

types of transformation and the considered T values. Once the link between T and σ is known, also the links of T with ξ (using again Eqs. (17) and (18)), F and L can be derived. Moreover, the link between T and ρ, E and ζ_i can be found with Eqs. (3), (14) and (32), respectively. Then the FRFs of Eqs. (28), (29) and (30) can be estimated. This procedure allows finding the FRFs for each T value and each transformation. These FRFs are then used to estimate h through Eqs. (4) to (12). The knowledge of h then allows for finding the relationship between i and T by means of Eq. (1) for the two transformations. The knowledge of these relationships enables estimating the wire temperature and its FRFs when a given value of i is set by the user.

4. Model validation by means of experiments

This section addresses the validation of the previous models by means of experiments on tailored set-ups. Section 4.1 presents the tests for the beam-based ATMD, while Section 4.2 those related to the wire-based ATMD.

4.1. Tests with a beam-based ATMD

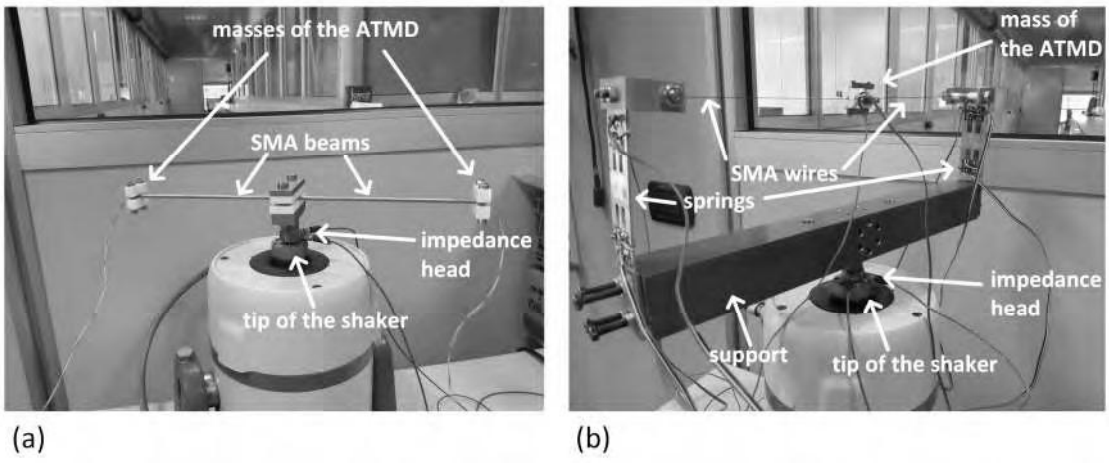

Figure 4: Experimental set-ups: beam-based ATMD (a) and wire-based ATMD (b).

Table 2: Identified/nominal parameter values for the SMA elements.

	Beam	Wire
A_s [°C]	55.0	68.6
A_f [°C]	65.0	78.9
M_s [°C]	40.0	55.2
M_f [°C]	28.5	42.7
C_A [MPa/°C]	-	9.90
C_M [MPa/°C]	-	6.83
H^cur [-]	-	$4.39{\cdot}10^{-2}$
α [°C^{-1}]	-	10^{-6}
E_m [GPa]	32.3	32.1
E_a [GPa]	52.7	39.5
ρ_m [Ωm]	$90{\cdot}10^{-8}$	$110{\cdot}10^{-8}$
ρ_a [Ωm]	$100{\cdot}10^{-8}$	$100{\cdot}10^{-8}$
$\zeta_{1,\mathrm{m}}$ [-]	$1.22{\cdot}10^{-2}$	$0.60{\cdot}10^{-2}$
$\zeta_{1,\mathrm{a}}$ [-]	$0.90{\cdot}10^{-2}$	$0.40{\cdot}10^{-2}$

Table 3: Nominal values of the imposed electrical current i during tests presented in Figs. 5 and 9 and consequent electrical power P values calculated as $P = iV$, where V is the voltage provided by the power supply and measured across the electrical circuit made from the electrical series of either the two beams or the two wires.

Beam				Wire			
Heating		Cooling		Heating		Cooling	
i [A]	P [W]	i [A]	P [W]	i [A]	P [W]	i [A]	P [W]
0.00	0.00	7.50	12.00	0.00	0.00	1.85	7.95
1.00	0.10	7.00	10.50	0.25	0.42	1.50	5.55
2.00	0.60	4.00	3.20	0.50	2.20	1.00	2.85
3.00	1.65	3.00	1.50	0.75	2.95	0.90	2.43
4.00	3.20			0.90	2.70		
5.00	5.00			1.00	2.90		
6.00	7.50			1.10	3.63		
6.50	8.77			1.25	4.00		
7.00	10.50			1.50	5.55		
7.50	12.00			1.85	7.95		

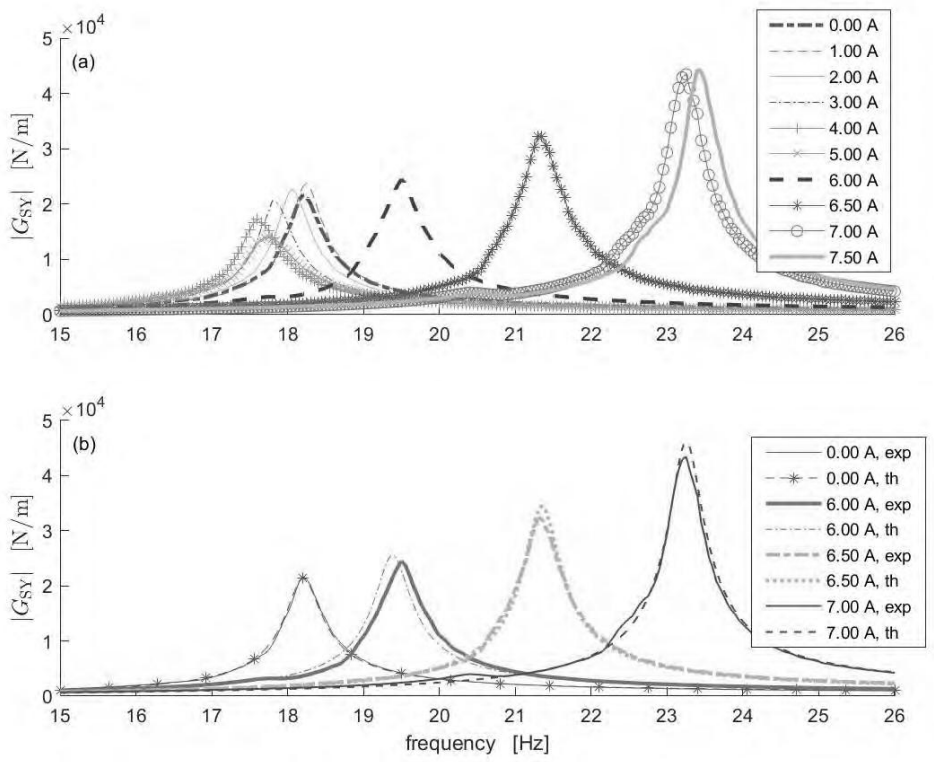

Figure 5: Experimental amplitudes of FRFs G_{SY} while heating the beams (see Table 3) (a) and comparison between experimental (exp) and theoretical (th) FRF amplitudes (b).

The set-up is made from two NiTiNOL beams, both characterised by a length equal to 140 mm and a circular hollow cross-section with an outside diameter of 4 mm and a thickness of 0.5 mm. At the two ends, there are two masses (0.176 kg each) made from plastic. The two beams are mounted on an electro-dynamic shaker which provides the input in the form of random signal between 4 and 100 Hz with a root mean square (RMS) value usually close to 5 m/s^2. The h values for both martensite and austenite were estimated as approximately equal to 15 W/(m^{2}K) with the approach described in Section 3.1. An impedance head was placed between the shaker and the clamping system, measuring the vibration in input to the ATMD and the consequent force exerted by the beams on the

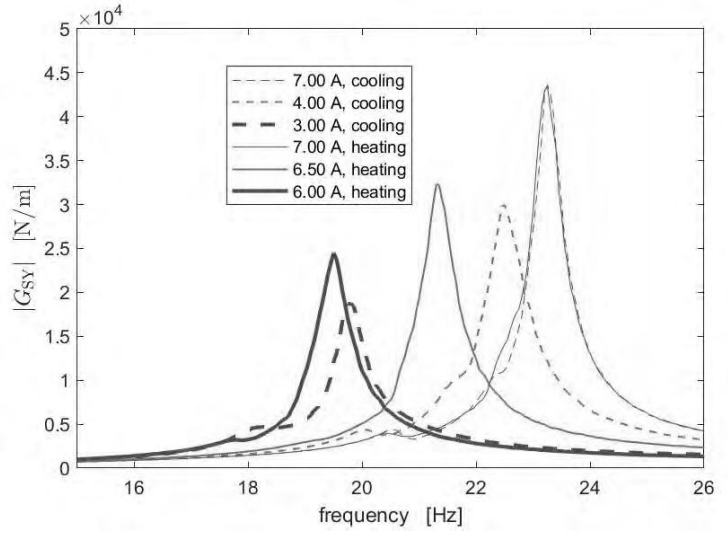

Figure 6: Experimental amplitudes of FRFs G_{SY} while either heating or cooling the beams (see Table 3).

shaker. The two beams were electrically connected in series to a power supply which made electrical current flow in the circuit. The whole set-up is presented in Fig. 4a. The main parameters of the NiTiNOL beams are reported in Table 2.

Figure 5a shows the experimental FRFs G_{SY} (after having removed the contribution of the clamping system and obtained using H_1 estimator [30]) for increasing values of current i applied to the beams, passing from martensite to austenite. The corresponding electrical power consumption P values are reported in Table 3. The figure evidences that no phase transition occurs for values of current up to 5 A (i.e., FRF peaks almost at the same frequency value). Over this threshold, the phase starts changing. It is thus possible to conclude that the phase transformation starts for values of i between 5 and 6 A. The model predicts the start of the phase transformation for i values not far from 5.5 A. Therefore, there is a good agreement with the experiments. During phase transformation, the peak height increases and the eigenfrequency moves towards higher frequency values, as expected from the previous models.

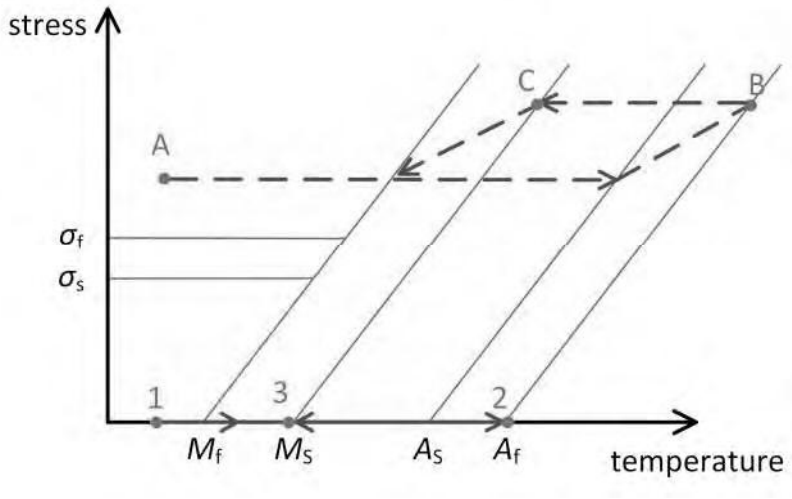

Figure 7: Heating/cooling paths followed by the SMA elements (solid line for beam and dashed line for wire) for going from ambient temperature to a a temperature where the transformation in AU is completed and, then, back to ambient temperature. The arrows indicate the paths followed increasing/decreasing the current i and, thus, the temperature T.

The austenite phase is reached for i approximately between 7 and 7.5 A and the model expectation is at 7 A, still with a good match. Figure 5b shows the comparison between some experimental and numerical FRFs, evidencing a good match.

Another interesting plot is that reported in Fig. 6, which shows that higher eigenfrequency values are obtained with lower electrical current i and power P values when cooling (i.e. passing from austenite to martensite), compared to heating (i.e. passing from martensite to austenite); see Table 3. This evidences the advantage of reaching a desired eigenfrequency value while cooling, that is mainly because M_s is lower than A_s (see Fig. 1; see also Section 5 for more details). Basically, this effect is mainly related to the material model (see Section 3.2). If one heats the SMA beam (increasing i) from ambient temperature until AU phase is reached (from point 1 to point 2 in Fig. 7), the eigenfrequency of the first mode (but the same applies to the eigenfrequencies of higher modes) gradually increases from a given value (generically defined as ω_1^{p1}) to a higher

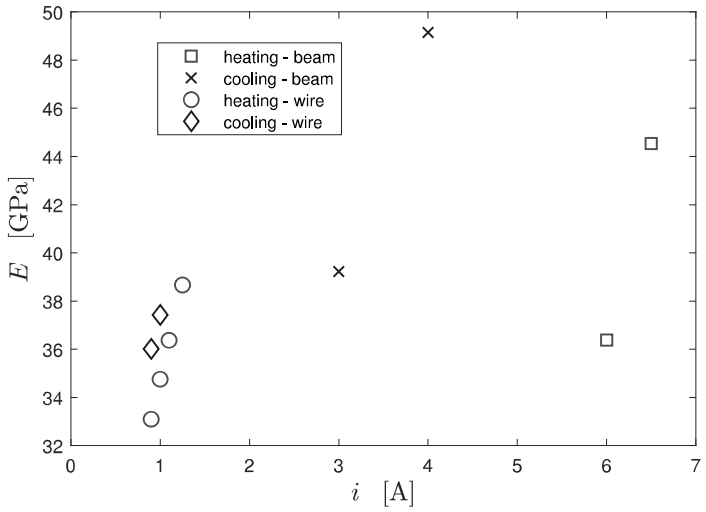

Figure 8: E values estimated through models for some tests in which the SMA beams/wires were in phase transition (see Table 3).

value $\omega_1^{\mathrm{p}2}$ during phase transformation (i.e., for $A_\mathrm{s} < T < A_\mathrm{f}$) because of the higher E value in AU than in martensite (see Table 2). If, then, i is decreased, also the temperature of the SMA element decreases. During the first part of the decrease (from point 2 to point 3 in Fig. 7), there is no change of phase and, thus, the change of eigenfrequency value is null (or, actually, slight). In point 3 of Fig. 7, the corresponding eigenfrequency value $\omega_1^{\mathrm{p}3}$ is equal to $\omega_1^{\mathrm{p}2}$. Hence, the same eigenfrequency value is obtained with a lower current value. Then, a further decrease of i (and, thus, of temperature T) generates a shift of the eigenfrequency towards $\omega_1^{\mathrm{p}1}$. Therefore, it is possible to mention that the same i value is able to give rise to different eigenfrequency values according to the sign of the change of i (and T) and also that cooling can provide eigenfrequency values as those obtained by heating, but with smaller values of i.

The FRFs in Fig. 6 related to cooling shows slightly lower peaks because of poorer capability of power supply to keep the nominal current value, generating broader peaks (this could be easily improved by implementing a feedback control on the action of the power supply, which instead worked in open loop in the presented tests).

Finally, Fig. 8 presents the values of E estimated through the model for some tests in which the SMA beams were in phase transition. Furthermore, the value of the non-dimensional damping ratio ζ_1 was estimated for the tests in which the beam was heated and in phase transition for different values of the electrical current i: at 6 A the value of ζ_1 was approximately equal to $1.19{\cdot}10^{-2}$, at 6.5 A approximately equal to $1.12{\cdot}10^{-2}$, and, finally, at 7 A about $0.92{\cdot}10^{-2}$.

4.2. Tests with a wire-based ATMD

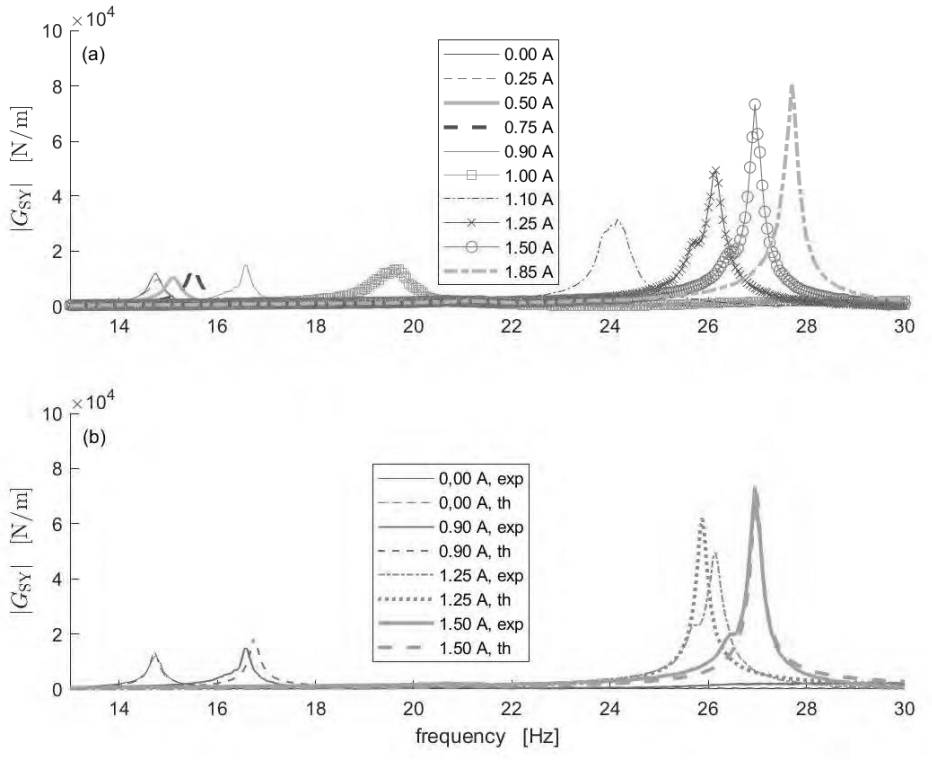

Figure 9: Experimental amplitudes of FRFs G_{SY} while heating the wires (see Table 3) (a) and comparison between experimental (exp) and theoretical (th) FRF amplitudes (b).

The set-up was made from NiTiNOL wires with a length of 143 mm each and a diameter of 0.5 mm. The central mass (0.018 kg) was made from plastic and steel. The springs were built using steel thin cantilever beams [18]. The

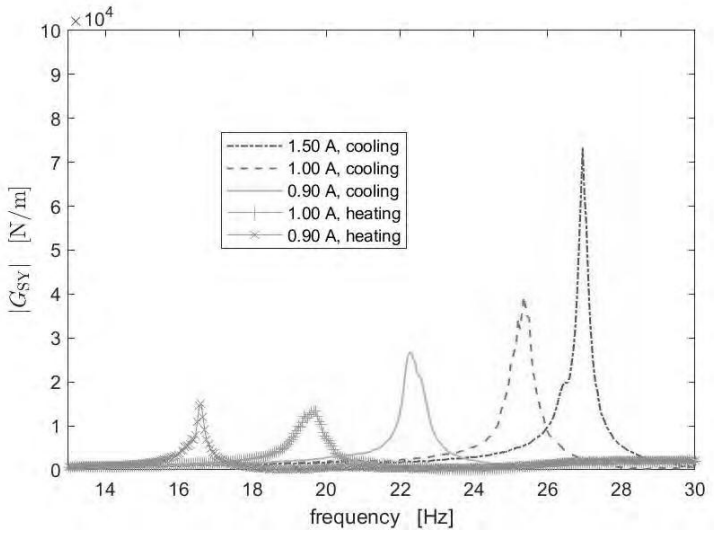

Figure 10: Experimental amplitudes of FRFs G_{SY} while either heating or cooling the wires (see Table 3).

whole set-up was mounted on a thick steel bar used only as a support. The random input was provided again with a shaker between 4 and 100 Hz, with an RMS value usually close to 0.5 m/s^2. In this case, the RMS was decreased compared to the case of the beam in order to have h values not too far between the two cases. In the wire case, the h value for martensite was estimated close to 50 W/(m^{2}K), and close to 75 W/(m^{2}K) for austenite. The whole set-up is presented in Fig. 4b and the main parameters of the NiTiNOL wires are reported in Table 2. It is also noticed that the beam-like springs were built such that the stress in the wire in martensite phase was approximately equal to 58.6 MPa and about 190.5 MPa in austenite phase.

Figure 9a shows the experimental FRFs G_{SY} (after having removed the contribution of the bar used for the connection to the shaker) for increasing values of current i applied to the beams. The corresponding P values are reported in Table 3. The figure evidences that no transition of material phase occurs for values of current up to approximately 0.5 A (i.e., FRF peaks almost at the same frequency value) and, over this threshold, the phase starts changing. According

to Fig. 9, the start of the phase transformation occurs between 0.5 and 0.9 A. The model predicts the start at about 0.8 A, showing a satisfactory match. During phase transformation, the peak height increases and the eigenfrequency moves towards higher frequency values, as expected. The austenite phase is reached for i not far from 1.85 A, and the model predicts the transformation stop for i approximately equal to 1.3 A, with an acceptable approximation. Figure 9b shows the comparison between experimental and numerical FRFs while heating. The match during phase transformation is not as satisfactory as in the case of the beam ATMD. This is again mainly related to the power supplier used, which could not maintain a constant current value with enough accuracy. Indeed, in this case, even slight changes of the current (e.g., 0.05 A) were able to generate non-negligible FRF changes. These changes are evident in Fig. 9b, where some resonance peaks are broad because of a non-constant current value. This evidences the need of a feedback control on i for a fine tuning of the ATMD eigenfrequency in real applications. Even if the match between theoretical and experimental FRFs is not as good as in the case of the beam-based ATMD, the model proves to correctly describe the trend of the eigenfrequency values and of the corresponding peak height.

Figure 10 confirms a fact already noticed for the beam-based ATMD (see Section 4.1): cooling allows obtaining higher eigenfrequency values with a lower i value (and, thus, electric power P; see Table 3), compared to heating, as expected because of the hysteretic behaviour in the temperature-stress plane (see also Section 5 for more details). Indeed, heating from ambient temperature to austenite (i.e., from point A to point B in Fig. 7), the first eigenfrequency (the same occurs for higher eigenfrequencies) gradually increases from ω_1^{pA} to ω_1^{pB} during phase transformation because of the stress increase in the SMA wire generated by the phase transition from DM to AU. Then, lowering i, T decreases and point C in Fig. 7 is reached, where ω_1^{pC} is almost equal (actually, slightly different, see Section 3.2) to ω_1^{pA} because the stress does not change significantly due to the fact that the material phase is not changing. Then, a further decrease of i allows lowering the stress value and, therefore, the eigenfrequency value

Table 4: Values of RMS of $y(t)$ and frequency band of the same signal.

	RMS of $y(t)$ [m]	lower frequency bound [Hz]	higher frequency bound [Hz]
ATMDs tuned at 15 Hz	0.30×10^{-3}	5	38
ATMDs tuned at 35 Hz	0.25×10^{-3}	10	45

Table 5: Parameter values for both SMA beams and wires used for the comparisons.

Parameter	Value
A_s [°C]	68.6
A_f [°C]	78.9
M_s [°C]	55.2
M_f [°C]	42.7
C_A [MPa/°C]	9.90
C_M [MPa/°C]	6.83
H^cur [-]	$4.39{\cdot}10^{-2}$
α [°C^{-1}]	10^{-6}
E_m [GPa]	32.1
E_a [GPa]	39.5
ρ_m [Ωm]	$90{\cdot}10^{-8}$
ρ_a [Ωm]	$100{\cdot}10^{-8}$

towards ω_1^{pA} because of the phase transition from AU to DM.

Finally, as already done for the beam, Fig. 8 shows the values of E estimated through the model for some tests in which the SMA wire was in phase transition.

5. Comparison of beam- and wire-based ATMDs

The models validated in the previous section are now employed to the aim of comparing the two types of ATMD. As mentioned in Section 1, the comparison is carried out in terms of:

- adaptation capability which indicates how much the ATMD eigenfrequency can be changed;
- force exerted by the ATMD on the PS, which is related to the attenuation performance which can be achieved;
- power consumption related to the need of having current flowing through the SMA elements.

To perform a comparison, the two types of ATMD are initially tuned at the same frequency value (i.e., first eigenfrequency of the ATMD tuned to a given predefined value). The cross-section of the beam- and wire-based ATMDs are the same as those considered in the previous experiments: diameter of 0.5 mm for the wire and circular hollow section with an outside diameter of 4 mm and a thickness of 0.5 mm for the beam. These values have been used because they can be easily found in commercial products. However, the previous models can be employed for simulations with different cross-sections (i.e., different diameter values but also different cross-section shapes for the beam).

Moreover, the comparison is performed with the following two constraints:

- the two ATMDs have the same mass (global mass given by the sum of concentrated masses and the mass of the wires/beams, referred to as M_{tot}). The two constraints on both the eigenfrequency value and the total mass involve that the length of the ATMD is adjusted in order to meet the two of them. It is noticed that the concentrated mass value ranges approximately between 0.02 and 0.30 kg for the wire ATMD and between about 0 and 0.15 kg for the beam ATMD in the simulations;
- the RMS value of the input random signal $y(t)$ is the same for the wire- and beam-based ATMDs. Furthermore, also the frequency band of the disturbance is the same (see Table 4).

In all the simulations, the value of ζ_1 is set to 10^{-2} for both the ATMDs and the value of the spring constant K for the wire-based ATMD is set in order to

satisfy the constraint of having a stress value equal to 50 MPa at environmental temperature in DM and 200 MPa in AU. Finally, the same material parameter values were used for the two ATMDs and they are reported in Table 5.

At first, the two ATMDs are compared in terms of adaptation capability (Section 5.1) and, then, in terms of force exerted (Section 5.2) and power consumption (Section 5.3).

5.1. Comparison in terms of adaptation capability

The two ATMDs are initially tuned at either 15 or 35 Hz at environmental temperature. Then, current is increased until complete transformation in AU occurs. To quantify the adaptation capability comparison, the ratio R_{eig} is defined as:

$$R_{\text{eig}} = \frac{\omega_1^{\text{A,wire}} - \omega_1^{\text{M,wire}}}{\omega_1^{\text{A,beam}} - \omega_1^{\text{M,beam}}} \tag{33}$$

which is the ratio between the adaptation span of the first eigenfrequency (eigenfrequency in AU minus eigenfrequency in martensite at environmental temperature) for the wire ATMD and that for the beam ATMD. It is noticed that in these simulations both $\omega_1^{\text{M,beam}}$ and $\omega_1^{\text{M,wire}}$ are equal to either $2\pi \times 15$ or $2\pi \times 35$ rad/s.

For the two initial eigenfrequency values (i.e., 15 and 35 Hz) and all the considered M_{tot} values (i.e., approximately between 0.02 and 0.3 kg), the value of R_{eig} results approximately equal to 9.5, evidencing that the wire-based ATMD provides a much larger adaptation capability, as already evidenced by the experiments (compare Figs. 5a and 9a).

5.2. Comparison in terms of exerted force

To the purpose of exerted force comparison (and also for the comparison in terms of power consumption, see Section 5.3), it is important to evidence that different tuning strategies are possible. The starting point is the eigenfrequency range covered by the beam-based ATMD. Indeed, according to Section 5.1, it is the layout with the narrower range of frequency adaptation, varying from

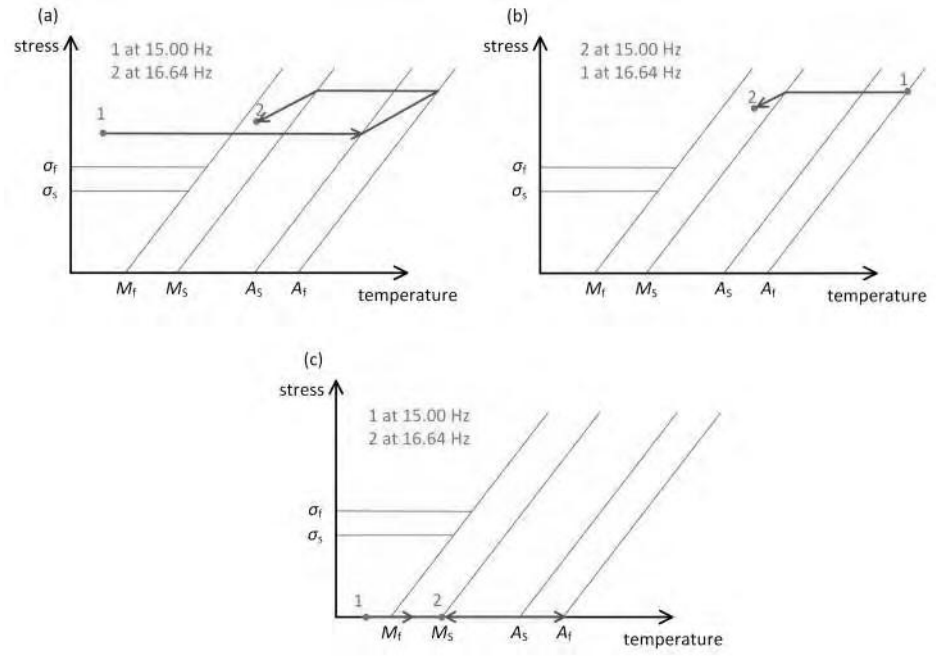

Figure 11: Paths followed by the SMA elements for reaching eigenfrequency at 15.00 Hz (or 35.00 Hz) and 16.64 Hz (or 38.82 Hz). Wire-based ATMD with tuning approach 1 (a), wire-based ATMD with tuning approach 2 (b) and beam-based ATMD (c). The arrows indicate the paths followed increasing/decreasing the temperature.

$\omega_1^{\mathrm{M,beam}}$ to $\omega_1^{\mathrm{A,beam}}$. The wire-based ATMD can be tuned correspondingly in the two following ways:

- it is initially tuned to $\omega_1^{\mathrm{M,beam}}$ at environmental temperature (i.e. $\omega_1^{\mathrm{M,wire}}$=$\omega_1^{\mathrm{M,beam}}$) (point 1 in Fig. 11a). For the considered cases, the corresponding numerical values are 15 and 35 Hz (see Sections 5 and 5.1). Then, the temperature of the wire is increased until complete AU transformation is obtained. Being $\omega_1^{\mathrm{A,wire}} \gg \omega_1^{\mathrm{A,beam}}$, the temperature of the wire is then decreased. When transformation to DM starts, the value of ω_1^{wire} significantly decreases, where ω_1^{wire} without superscripts A and M refers to a generic phase situation in which AU and DM are both present. The temperature decrease is stopped when ω_1^{wire}= $\omega_1^{\mathrm{A,beam}}$ (point 2 in Fig. 11a). For the

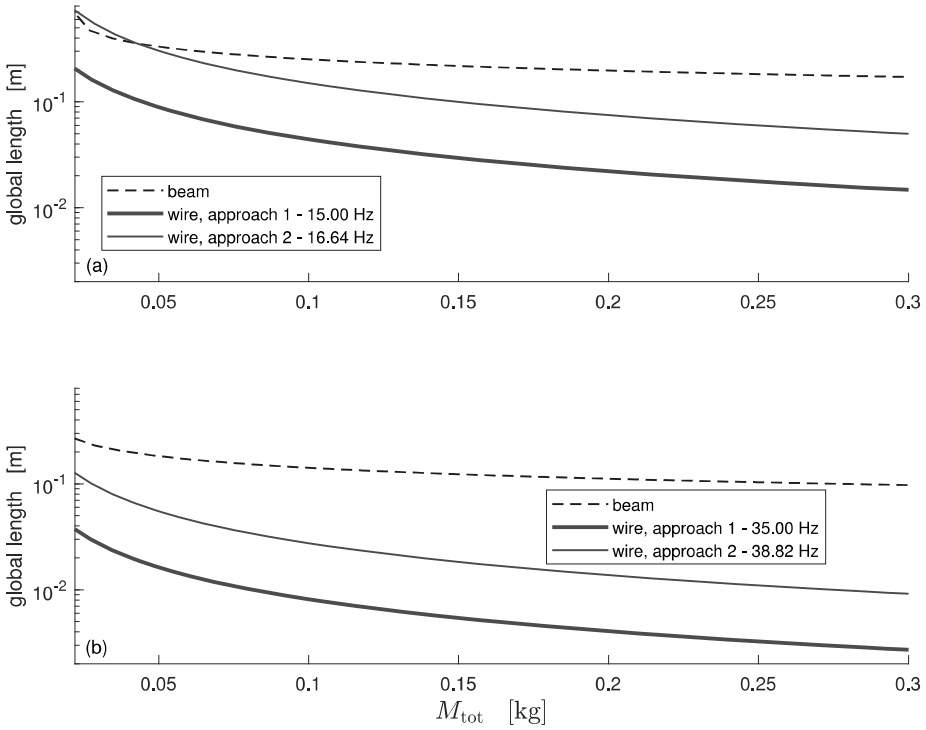

Figure 12: Relationship between M_{tot} value and ATMD global length L_{tot} for the ATMDs working between 15.00 and 16.64 Hz (a) and those working between 35.00 and 38.82 Hz (b).

considered cases, the frequency values result equal to approximately 16.64 and 38.82 Hz. Therefore, the comparison of the two ATMD layouts is performed at 15 and 16.64 Hz in one case and at 35 and 38.82 Hz in the other.

- it is initially tuned to $\omega_1^{\mathrm{A,beam}}$ when in AU (i.e. $\omega_1^{\mathrm{A,wire}}$=$\omega_1^{\mathrm{A,beam}}$, point 1 in Fig. 11b). For the considered cases, the corresponding numerical values are 16.64 and 38.82 Hz. Then, the temperature of the wire is decreased. When transformation to DM starts, the value of ω_1^{wire} significantly decreases. The temperature decrease is stopped when ω_1^{wire}= $\omega_1^{\mathrm{M,beam}}$ (point 2 in Fig. 11b). For the considered cases, the frequency values result equal to 15 and 35 Hz. Therefore, the comparison of the two ATMD layouts is performed again at 15 and 16.64 Hz in one case and at 35 and 38.82 Hz

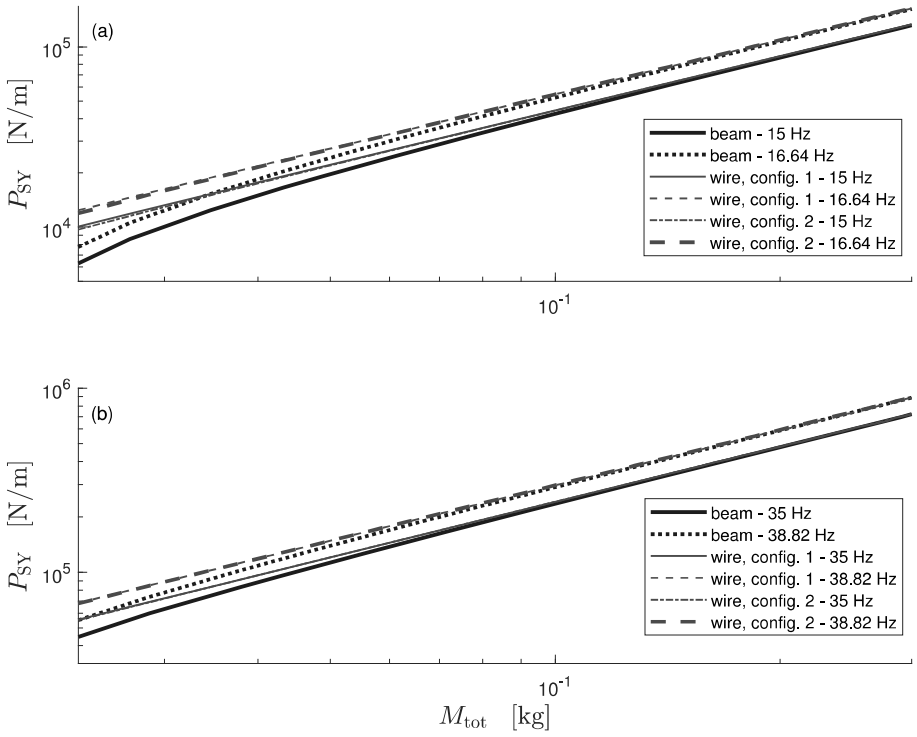

Figure 13: Trend of the peak values of $|G_{SY}|$, named P_{SY}, for all the considered cases for the ATMDs working between 15.00 and 16.64 Hz (a) and those working between 35.00 and 38.82 Hz (b).

in the other.

The two above-mentioned tuning approaches for the wire-ATMD will be referred to as approach 1 and 2, respectively.

First of all, the relationship between M_{tot} and the corresponding global length L_{tot} of the ATMD is presented in Fig. 12 for all the different cases (it is remembered that the global length is $2L$ for the beam, see Section 3.3.1, and L for the wire, see Section 3.3.2; see also Fig. 2). It emerges that approach 1 provides shorter ATMD configurations compared to approach 2 for the wire-based device. Furthermore, the wire-based layout results shorter compared to the beam-like ATMD. Even if the advantage provided by the wire is evident in terms of bulk, it is worth noticing that for larger and larger M_{tot} values and

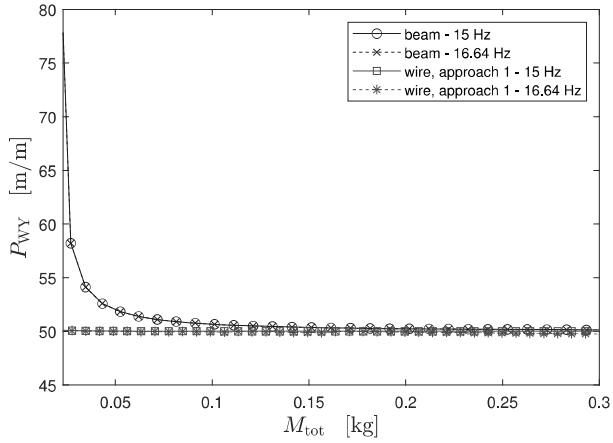

Figure 14: Trend of the peak values of $|G_{\mathrm{WY}}|$, named P_{WY}, for the ATMDs working between 15.00 and 16.64 Hz. The results related to apporach 2 for tuning the wire-based ATMD are not presented here because they are almost equal to those of apporach 1. It is noticed that the two curves related to the beam-ATMD are almost superimposed. The same occurs for the curves of the wire-ATMD.

higher and higher eigenfrequency values, the length of the wire-ATMD becomes too short and, thus, not feasible. Therefore, when the needed eigenfrequency value increases and a large M_{tot} value is required in order to increase the exerted force (see further in this sub-section), the wire-based ATMD could become not feasible and the only usable layout is that based on the beams. Furthermore, in a situation like this, tuning approach 2 could become advantageous compared to approach 1. Furthermore, it is noticed that additional possibilities for still using the wire-based ATMD with the tuning apporach 1 are to either employ a wire with a larger diameter or add wires in parallel.

Figure 13 shows the peak values of $|G_{\mathrm{SY}}|$ (i.e., the values at resonance), named P_{SY}, for all the considered cases. As expected from the experimental results, the mentioned peaks are higher at higher frequency (compare plots a and b in Fig. 13 and also the curves related to different frequency values in the same plot). Furthermore, the differences for the wire-ATMD between approach 1 and 2 are not significant. Wire- and beam-based ATMD provide similar forces, when the M_{tot} value increases, while higher forces are produced by the wire-

based ATMD for low values of M_{tot}. Another interesting result is provided in Fig. 14, where the peak of $|G_{\mathrm{WY}}|$ (considering the displacement of the central mass for the wire-based ATMD and of mass at the beam tip for the beam-based ATMD), named P_{WY}, is shown for the case of the ATMD working between 15 and 16.64 Hz, chosen as an example. At high M_{tot} value, the displacements tend to be equal, as in the case of the exerted force, but, at low values of M_{tot}, the wire-based ATMD tends to move less, even if it provides higher forces. This is also related to the different global lengths of the ATMDs (see Fig. 12).

5.3. Comparison in terms of power consumption

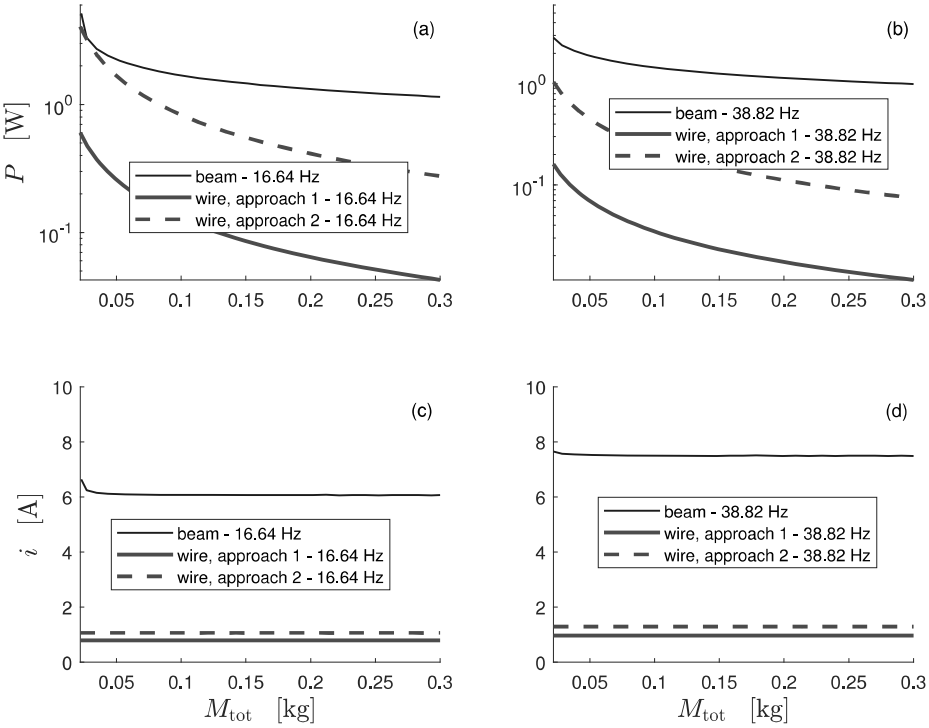

Figure 15: Trend of P as a function of M_{tot} for the ATMD working between 15.00 and 16.64 Hz (a) and for that working between 35.00 and 38.82 Hz (b). Corresponding trend of i as a function of M_{tot} for the ATMD working between 15.00 and 16.64 Hz (c) and for that working between 35.00 and 38.82 Hz (d).

This subsection aims at comparing the two ATMD layouts in terms of power

consumption, also considering the electric current value involved.

The comparison is carried out in terms of power and current needed to bring the ATMD at the maximum eigenfrequency value (i.e., 16.64 and 38.82 Hz for the two considered cases). Regarding the wire-based ATMD, these eigenfrequency values correspond to point 2 in Fig. 11a and point 1 in Fig. 11b for tuning approach 1 and 2, respectively. Regarding the beam-based ATMD, the considered point in the temperature-stress plot is point 2 in Fig. 11c. Point 2 is reached after increasing the temperature from environmental temperature (point 1 in the figure) until transformation in AU is completed and, then, decreasing temperature and stopping the decrease just before transformation to TM starts (point 2). On the whole horizontal part of path leading to point 2 from AU phase, temperature changes while exerted force and eigenfrequency do not because the model related to the beam does not consider thermal expansion (its influence is assumed as negligible); see Section 3.

No comparison is performed at 15 and 35 Hz because there is no power consumption for the beam- and the wire-ATMD with tuning approach 1 in these cases.

Figures 15a and b show the power consumption P as a function of M_{tot} for all the considered cases, while Figs. 15c and d show the trend of i. Tuning approaches 1 and 2 for the wire-based ATMD show significantly different values of both P and i, especially at low values of M_{tot}, evidencing the benefit provided by tuning approach 1.

Addressing the comparison between wire- and beam-ATMD, the former results much less expensive in terms of electrical consumption. Often, the power consumption required by the wire-ATMD (with tuning approach 1) is almost ten times lower than that of the beam-ATMD.

Finally, it is noticed that another tuning strategy was considered for the wire-ATMD. This is equal to tuning strategy 1, with the exception that the value of the spring elements K was lowered so that the ATMD only worked between either 15.00 and 16.64 Hz or 35.00 and 38.82 Hz. The results associated to this further case are not shown in the paper because they lead to slightly worse

results in terms of power consumption, compared to tuning strategy 1, and to similar results in terms of exerted peak force P_{SY}.

6. Conclusion

The paper addressed the comparison between the two main layouts (wire-based and beam-based) for developing adaptive tuned mass dampers based on shape memory alloys. To perform such a comparison, the models of the two types of adaptive tuned mass dampers were developed. These models allow for reconstructing the device dynamics as function of the provided electrical current. The models require in input the parameters of the shape memory alloy used, the geometrical features and the input vibration. An experimental validation was carried out for the models of both the devices, with satisfactory results.

The wire-based layout shows much greater adaptation capability and much smaller electrical power consumption compared to the beam-layout. The developed models allowed quantifying these differences, which were shown to be able to reach even one order of magnitude. Regarding the force exerted on the primary system by the tuned mass damper, the two layouts are not so different, even if the wire-based layout is able to provide a larger force compared to the beam-based configuration when the mass of the tuned mass damper is small. Furthermore, in such a case, the global size of the wire-based device is consistently lower than that of the beam-based layout and it shows smaller oscillations.

Nevertheless, some disadvantages related to the use of the wire-based layout must be evidenced as well. The first one is that it has a higher construction complexity, e.g., due to the presence of additional elastic elements, the need of either two connection points or an additional frame. Furthermore, when the value of the required eigenfrequency increases, the size of the wire-based tuned mass damper can become so small that it is not feasible in practice. Finally, the wire layout is more sensitive to electrical current changes and, therefore, more stringently requires the use of feedback control on the value of the supplied

electrical current.

Appendix A. FRFs for the beam-based ATMD

The solution of the problem in Eq. (22) can be found in different references (e.g., [27, 28]) and is in the following form:

$$\begin{aligned} w_{\mathrm{rel}}(x,t) = [B_1 \sin(\gamma x) + B_2 \cos(\gamma x) + B_3 \sinh(\gamma x) \\ + B_4 \cosh(\gamma x)][B_5 \cos(\Omega t) + B_6 \sin(\Omega t)] \end{aligned} \tag{A.1}$$

where $\gamma = \Omega^{(1/2)}[(\theta_{\mathrm{m}} A)/(EJ)]^{(1/4)}$, while B_1 to B_6 are constants to be determined. The boundary conditions of the problem are the following:

$$w_{\mathrm{rel}}(x,t) = 0, \ x = 0 \tag{A.2}$$

$$\frac{\partial w_{\mathrm{rel}}(x,t)}{\partial x} = 0, \ x = 0 \tag{A.3}$$

$$Z(x,t) = 0, \ x = L \tag{A.4}$$

$$Q(x,t) + M_{\mathrm{a}} \frac{\partial^2 w_{\mathrm{rel}}(x,t)}{\partial t^2} = 0, \ x = L \tag{A.5}$$

where M_{a} is the value of the additional mass (see Fig. 2a), that is considered as a concentrated mass for the sake of simplicity.

Considering that:

$$Q(x,t) = -EJ \frac{\partial^3 w(x,t)}{\partial x^3} \tag{A.6}$$

the use of these boundary conditions leads to the following matrix system:

$$\mathbf{A}_{\mathrm{b}} \mathbf{U}_{\mathrm{b}} = [0 \ \ 0 \ \ 0 \ \ 0]^{\mathrm{T}} \tag{A.7}$$

where T indicates the transposed matrix and:

$$\mathbf{A}_\mathrm{b} = \begin{bmatrix} 0 & 1 & 0 & 1 \\ 1 & 0 & 1 & 0 \\ -\sin(\gamma L) & -\cos(\gamma L) & \sinh(\gamma L) & \cosh(\gamma L) \\ -\tau\cos(\gamma L) + \lambda\sin(\gamma L) & \tau\sin(\gamma L) + \lambda\cos(\gamma L) & \tau\cosh(\gamma L) + \lambda\sinh(\gamma L) & \tau\sinh(\gamma L) + \lambda\cosh(\gamma L) \end{bmatrix} \tag{A.8}$$

$$\mathbf{U}_\mathrm{b} = [B_1 \;\; B_2 \;\; B_3 \;\; B_4]^\mathrm{T} \tag{A.9}$$

$$\tau = EJ\gamma^3, \;\; \lambda = \Omega^2 M_\mathrm{a} \tag{A.10}$$

The eigenfrequencies ω_i (and the corresponding γ_i values) of the beam can be found solving $\det(\mathbf{A}_\mathrm{b})=0$ for Ω. Then, using the obtained ω_i values in Eq. (A.7), setting one of the unknowns to a given value (e.g., $B_1=1$), and discarding one of the four scalar equations in Eq. (A.7) because of the additional constraint $\det(\mathbf{A}_\mathrm{b})=0$, it is possible to derive the other three unknowns and thus the mode shapes ϕ_i associated to ω_i:

$$\phi_i(x) = [B_{1,i}\sin(\gamma_i x) + B_{2,i}\cos(\gamma_i x) + B_{3,i}\sinh(\gamma_i x) + B_{4,i}\cosh(\gamma_i x)] \tag{A.11}$$

It is now possible to use the modal coordinates q_i to express $w_\mathrm{rel}(x,t)$:

$$w_\mathrm{rel}(x,t) = \sum_{i=1}^{n} \phi_i(x) q_i(t) \tag{A.12}$$

where n is the number of modes (that is infinite in theory). Defining the velocity of the mass as:

$$V_\mathrm{mass} = \frac{\partial w_\mathrm{rel}(x,t)}{\partial t}\Big|_{x=L} \tag{A.13}$$

$$\mathbf{\Phi}(x) = [\phi_1(x), ..., \phi_i(x), ..., \phi_n(x)]^\mathrm{T} \tag{A.14}$$

$$\mathbf{q}(t) = [q_1(t), ..., q_i(t), ..., q_n(t)]^\mathrm{T} \tag{A.15}$$

and relying on the modal approach, the kinetic energy E_k can be derived:

$$\begin{gathered} E_\mathrm{k} = \frac{1}{2}\left[\int_0^L \theta_\mathrm{m} A \left(\frac{\partial w_\mathrm{rel}(x,t)}{\partial t}\right)^2 \mathrm{d}x + M_\mathrm{a} V_\mathrm{mass}^2\right] = \\ \frac{1}{2}\dot{\mathbf{q}}^\mathrm{T}(t)\left[\int_0^L \theta_\mathrm{m} A \boldsymbol{\Phi}(x)\boldsymbol{\Phi}^\mathrm{T}(x)\mathrm{d}x + M_\mathrm{a}\boldsymbol{\Phi}(L)\boldsymbol{\Phi}^\mathrm{T}(L)\right]\dot{\mathbf{q}}(t) \\ = \frac{1}{2}\dot{\mathbf{q}}^\mathrm{T}(t)\mathbf{M}\dot{\mathbf{q}}(t) \end{gathered} \tag{A.16}$$

Given the orthogonality of the vibration modes, $\mathbf{M}$ results being a diagonal matrix, having the modal masses m_i on the diagonal. Similarly, the modal stiffness values k_i can be obtained writing the potential energy relying on the modal approach. Finally, it is possible to derive the Lagrangian components $\mathbf{L}$ of the external forces (see Eq. (22)). Assuming a mono-harmonic law for $y(t)$ (at Ω, with amplitude y_0), the following expression is derived:

$$\mathbf{L}(t) = \left[\theta_\mathrm{m} A \int_0^L \boldsymbol{\Phi}(x)\mathrm{d}x + M_\mathrm{a}\boldsymbol{\Phi}(L)\right]\Omega^2 y_0 \mathrm{e}^{(\mathrm{j}\Omega t)} \tag{A.17}$$

Applying the Lagrange's equation, it is then possible to express the system dynamics with n single-degree-of-freedom equations:

$$m_i\ddot{q}_i(t) + k_i q_i(t) = \left[\theta_\mathrm{m} A \int_0^L \phi_i(x)\mathrm{d}x + M_\mathrm{a}\phi_i(L)\right]\Omega^2 y_0 \mathrm{e}^{(\mathrm{j}\Omega t)} \tag{A.18}$$

If proportional damping is now introduced in the mathematical treatment, the modal damping values c_i can be obtained writing the dissipation function relying on the modal approach and Eq. (A.18) can be modified as follows (see, e.g., [27, 28]):

$$m_i\ddot{q}_i(t) + c_i\dot{q}_i(t) + k_i q_i(t) = \left[\theta_\mathrm{m} A \int_0^L \phi_i(x)\mathrm{d}x + M_\mathrm{a}\phi_i(L)\right]\Omega^2 y_0 \mathrm{e}^{(\mathrm{j}\Omega t)} \tag{A.19}$$

Rearranging Eq. (A.19), moving to the frequency domain and considering again the absolute displacement $w(x,t)$ as a function of $y(t)$ and $w_\mathrm{rel}(x,t)$, the FRF between Y and W is obtained as in Eq. (23), with:

$$\omega_i = \sqrt{\frac{k_i}{m_i}}, \quad \zeta_i = \frac{c_i}{2m_i}\sqrt{\frac{m_i}{k_i}} \tag{A.20}$$

being ζ_i the non-dimensional damping ratio associated to the i-th eigenfrequency ω_i. Once the $G_{\mathrm{WY}}(x, \mathrm{j}\Omega)$ FRF is known, the FRF between Y and the action exerted on the PS can be derived, noticing that the two cantilever beams of Fig. 2b generate the same vertical action and two moments that cancel out each other. Being $s(t) = Q(x = 0, t)$ and considering Eq. (A.6), then:

$$s(t) = -2EJ \sum_{i=1}^{n} \frac{\mathrm{d}^3 \phi_i(x)}{\mathrm{d}x^3}\Big|_{x=0} q_i(t) \tag{A.21}$$

Therefore, the FRF between $Y(\mathrm{j}\Omega)$ and the vertical force exerted on the PS $S(\mathrm{j}\Omega)$ ($S(\mathrm{j}\Omega)$ is the Fourier transform of $s(t)$) is obtained as in Eq. (24).

Appendix B. FRFs for the wire-based ATMD

Analysing the free vibrations, the solution of the problem in Eq. (27) for each of the wires is in the following form (e.g. [27, 28]):

$$w_{\mathrm{rel}}(x, t) = [B_7 \mathrm{sin}(\chi x) + B_8 \mathrm{cos}(\chi x)][B_9 \mathrm{cos}(\Omega t) + B_{10} \mathrm{sin}(\Omega t)] \tag{B.1}$$

where $\chi = \Omega\sqrt{\theta_{\mathrm{m}} A/F}$, while B_7 to B_{10} are constants to be determined. Four boundary conditions are needed to find the eigenfrequencies and eigenvectors with the same approach used for the vibrating beam (see Section 3.3.1). Indeed, two unknown constants must be found for the left wire, and two for the right wire. These boundary conditions are that w_{rel} must be null at the two constraints, that w_{rel} must be the same for the two wires at the concentrated central mass, and finally the vertical dynamic equlibrium of the central mass. More details can be found in [19]. These boundary conditions lead to a matrix equation like that of Eq. (A.7), where:

$$\mathbf{A}_{\mathrm{b}} = \begin{bmatrix} 0 & 1 & 0 & 0 \\ 0 & 0 & \mathrm{sin}(\chi L/2) & \mathrm{cos}(\chi L/2) \\ \mathrm{sin}(\chi L/2) & \mathrm{cos}(\chi L/2) & 0 & -1 \\ -\chi F \mathrm{cos}(\chi L/2) & \chi F \mathrm{sin}(\chi L/2) & \chi F & \Omega^2 M_{\mathrm{a}} \end{bmatrix} \tag{B.2}$$

$$\mathbf{U}_\mathrm{b} = [B_7 \;\; B_8 \;\; B_{11} \;\; B_{12}]^\mathrm{T} \tag{B.3}$$

where B_{11} and B_{12} are the constants related to the mode shape of the second wire to be determined.

Once eigenfrequencies and eigenvectors have been deduced, modal coordinates can be introduced:

$$w_{\mathrm{rel},1}(x_1,t) = \sum_{i=1}^{n} \phi_{i,1}(x_1) q_i(t), \quad w_{\mathrm{rel},2}(x_2,t) = \sum_{i=1}^{n} \phi_{i,2}(x_2) q_i(t) \tag{B.4}$$

where the subscripts 1 and 2 refers to wire 1 (that between the left constraint and the central mass, see Fig. 2c) and 2 (that between the central mass and the right constraint, see Fig. 2c), respectively.

According to Eq. (B.4), kinetic energy can be written as follows:

$$\begin{gathered} E_\mathrm{k} = \tfrac{1}{2}\left[\int_0^{L/2} \theta_\mathrm{m} A \left(\tfrac{\partial w_{\mathrm{rel},1}(x_1,t)}{\partial t}\right)^2 \mathrm{d}x_1 + M_\mathrm{a} V_\mathrm{mass}^2 + \int_0^{L/2} \theta_\mathrm{m} A \left(\tfrac{\partial w_{\mathrm{rel},2}(x_2,t)}{\partial t}\right)^2 \mathrm{d}x_2\right] = \\ \tfrac{1}{2}\dot{\mathbf{q}}^\mathrm{T}(t)\left[\int_0^{L/2} \theta_\mathrm{m} A \boldsymbol{\Phi}_1(x_1)\boldsymbol{\Phi}_1^\mathrm{T}(x_1)\mathrm{d}x_1 + M_\mathrm{a}\boldsymbol{\Phi}_1(L/2)\boldsymbol{\Phi}_1^\mathrm{T}(L/2) + \int_0^{L/2} \theta_\mathrm{m} A \boldsymbol{\Phi}_2(x_2)\boldsymbol{\Phi}_2^\mathrm{T}(x_2)\mathrm{d}x_2\right]\dot{\mathbf{q}}(t) \\ = \tfrac{1}{2}\dot{\mathbf{q}}^\mathrm{T}(t)\mathbf{M}\dot{\mathbf{q}}(t) \end{gathered} \tag{B.5}$$

where $\boldsymbol{\Phi}_1$ and $\boldsymbol{\Phi}_2$ are related to the first and second wire, respectively, and:

$$\boldsymbol{\Phi}_1(x_1) = [\phi_{1,1}(x_1), ..., \phi_{i,1}(x_1), ..., \phi_{n,1}(x_1)]^\mathrm{T} \tag{B.6}$$

$$\boldsymbol{\Phi}_2(x_2) = [\phi_{1,2}(x_2), ..., \phi_{i,2}(x_2), ..., \phi_{n,2}(x_2)]^\mathrm{T} \tag{B.7}$$

Again $\mathbf{M}$ is a diagonal matrix with the modal mass values m_i on the diagonal. Finally, considering the Lagrangian components of the external forces (see Eq. (27)), n single-degree-of-freedom equations can be derived (also introducing proportional damping in the mathematical treatment):

$$\begin{gathered} m_i\ddot{q}_i(t) + c_i\dot{q}_i(t) + k_i q_i(t) = \\ \left[\theta_\mathrm{m} A\left(\int_0^{L/2} \phi_{i,1}(x_1)\mathrm{d}x_1 + \int_0^{L/2} \phi_{i,2}(x_2)\mathrm{d}x_2\right) + M_\mathrm{a}\phi_{i,1}(L/2)\right]\Omega^2 y_0 \mathrm{e}^{(\mathrm{j}\Omega t)} \end{gathered} \tag{B.8}$$

Using the same approach already adopted in Section 3.3.1, the FRF between Y and W is obtained for the first and the second wire are in form of Eqs. (28) and (29), respectively.

Being the amplitude of the vibration small by hypothesis, the following simplification can be taken into consideration for the force exerted by the ATMD on the PS $s(t)$:

$$\begin{aligned} s(t) \simeq F\frac{\partial w_{\mathrm{rel},1}(x_1,t)}{\partial x_1}\Big|_{x_1=0} - F\frac{\partial w_{\mathrm{rel},2}(x_2,t)}{\partial x_2}\Big|_{x_2=L/2} = \\ F\sum_{i=1}^{n}\left\{\left[\frac{\mathrm{d}\phi_{i,1}(x_1)}{\mathrm{d}x_1}\Big|_{x_1=0} - \frac{\mathrm{d}\phi_{i,2}(x_2)}{\mathrm{d}x_2}\Big|_{x_2=L/2}\right] q_i(t)\right\} \end{aligned} \tag{B.9}$$

According to Eqs. (B.8), (B.9) and (A.20), the FRF between $Y(\mathrm{j}\Omega)$ and the vertical force exerted on the PS $S(\mathrm{j}\Omega)$ ($S(\mathrm{j}\Omega)$ is the Fourier transform of $s(t)$) is as in Eq. (30).

References

References

[1] S. Krenk, Frequency analysis of the tuned mass damper, Journal of Applied Mechanics 72 (6) (2005) 936–942.

[2] S. Krenk, J. Høgsberg, Equal modal damping design for a family of resonant vibration control formats, Journal of Applied Mechanics 19 (9) (2013) 1294–1315.

[3] L. Zhang, L. Hong, J. S. Dhupia, S. Johnson, Z. Qaiser, Z. Zhou, A novel semi-active tuned mass damper with a continuously tunable stiffness, Proceedings of the Institution of Mechanical Engineers, Part C: Journal of Mechanical Engineering Science (2022) in press-doi:10.1177/09544062221119925.

[4] M. Brennan, Actuators for active control-tunable resonant devices, Applied Mechanics and Engineering 5 (1) (2000) 63–74.

[5] O. Heuss, R. Solloum, D. Mayer, T. Melz, Tuning of a vibration absorber with shunted piezoelectric transducers, Archive of Applied Mechanics 86 (2016) 1715–1732.

[6] G. M. Chatziathanasiou, N. A. Chrysochoidis, D. A. Saravanos, A semi-active shunted piezoelectric tuned mass damper for robust vibration control, Journal of Vibration and Control (2021) in press-doi:10.1177/10775463211026487.

[7] G. M. Chatziathanasiou, N. A. Chrysochoidis, C. S. Rekatsinas, D. A. Saravanos, A semi-active shunted piezoelectric tuned-mass-damper for multimodal vibration control of large flexible structures, Journal of Sound and Vibration 537 (2022) 117222. doi:10.1016/j.jsv.2022.117222.

[8] F. Weber, C. Boston, M. Maślanka, An adaptive tuned mass damper based on the emulation of positive and negative stiffness with an MR damper, Smart Materials and Structures 20 (1) (2011) 015012. doi:10.1088/0964-1726/20/1/015012.

[9] F. Weber, M. Maślanka, Frequency and damping adaptation of a TMD with controlled MR damper, Smart Materials and Structures 21 (5) (2012) 055011. doi:10.1088/0964-1726/21/5/055011.

[10] M. Acar, C. Yilmaz, Design of an adaptive–passive dynamic vibration absorber composed of a string–mass system equipped with negative stiffness tension adjusting mechanism, Journal of Sound and Vibration 332 (2) (2013) 231–245. doi:10.1016/j.jsv.2005.01.018.

[11] T. Long, M. J. Brennan, S. J. Elliott, Design of smart machinery installations to reduce transmitted vibrations by adaptive modification of internal forces, Proceedings of the Institution of Mechanical Engineers, Part I: Journal of Systems and Control Engineering 212 (3) (1998) 215–228. doi:10.1243/0959651981539415.

[12] F. Casciati, L. Faravelli, C. Fuggini, Cable vibration mitigation by added sma wires, Acta Mechanica 195 (1-4) (2008) 141–155. doi:10.1007/s00707-007-0541-x.

[13] L. Dieng, G. Helbert, S. Chirani, T. Lecompte, P. Pilvin, Use of shape memory alloys damper device to mitigate vibration amplitudes of bridge cables, Engineering Structures 56 (2013) 1547–1556. doi:10.1016/j.engstruct.2013.07.018.

[14] F. Santos, J. Nunes, Toward an adaptive vibration absorber using shape-memory alloys, for civil engineering applications, Journal of Intelligent Material Systems and Structures 29 (5) (2018) 729–740. doi:10.1177/1045389X17721031.

[15] K. Williams, G. Chiu, R. Bernhard, Adaptive-Passive Absorbers Using Shape-Memory Alloys, Journal of Sound and Vibration 249 (5) (2002) 835–848. doi:10.1006/jsvi.2000.3496.

[16] E. Rustighi, M. J. Brennan, B. R. Mace, A shape memory alloy adaptive tuned vibration absorber: design and implementation, Smart Materials and Structures 14 (1) (2005) 19–28. doi:10.1088/0964-1726/14/1/002.

[17] E. Rustighi, M. J. Brennan, B. R. Mace, Real-time control of a shape memory alloy adaptive tuned vibration absorber, Smart Materials and Structures 14 (6) (2005) 1184–1195. doi:10.1088/0964-1726/14/6/011.

[18] M. Berardengo, A. Cigada, F. Guanziroli, S. Manzoni, Modelling and control of an adaptive tuned mass damper based on shape memory alloys and eddy currents, Journal of Sound and Vibration 349 (2015) 18–38. doi:10.1016/j.jsv.2015.03.036.

[19] M. Berardengo, G. Della Porta, S. Manzoni, M. Vanali, A multi-modal adaptive tuned mass damper based on shape memory alloys, Journal of Intelligent Material Systems and Structures 30 (4) (2019) 536–555. doi:10.1177/1045389X18818388.

[20] B. Tiseo, A. Concilio, S. Ameduri, A. Gianvito, A shape memory alloys based tunable dynamic vibration absorber for vibration tonal control, Journal of Theoretical and Applied Mechanics 48 (2010) 135–153.

[21] M. A. Savi, A. S. De Paula, D. C. Lagoudas, Numerical Investigation of an Adaptive Vibration Absorber Using Shape Memory Alloys, Journal of Intelligent Material Systems and Structures 22 (1) (2010) 67–80. doi:10.1177/1045389X10392612.

[22] R. A. Aguiar, M. A. Savi, P. M. Pacheco, Experimental investigation of vibration reduction using shape memory alloys, Journal of Intelligent Material Systems and Structures 24 (2) (2012) 247–261. doi:10.1177/1045389X12461696.

[23] Y. Mani, M. Senthilkumar, Shape memory alloy based adaptive-passive dynamic vibration absorber for vibration control in piping applications, Journal of Vibration and Control 21 (9) (2015) 1838–1847. doi:10.1177/1077546313492183.

[24] D. Lagoudas, Shape memory alloys: modeling and engineering applications, Springer, 2008.

[25] M. Collet, E. Foltête, C. Lexcellent, Analysis of the behavior of a shape memory alloy beam under dynamical loading, European Journal of Mechanics, A/Solids 20 (4) (2001) 615–630. doi:10.1016/S0997-7538(01)01159-7.

[26] Y. Çengel, Introduction to Thermodynamics and Heat Transfer, 2nd Edition, McGraw-Hill, 2009.

[27] L. Meirovitch, Fundamentals of Vibrations, McGraw-Hill, 2001.

[28] F. Cheli, G. Diana, Advanced Dynamics of Mechanical Systems, Springer, 2015.

[29] B. Gómez, C. Repetto, C. Stia, R. Welti, Oscillations of a string with concentrated masses, European Journal of Physics 28 (5) (2007) 961–975. doi:10.1088/0143-0807/28/5/019.

[30] A. Brandt, Noise and Vibration Analysis – Signal Analysis and Experimental Procedures, John Wiley and Sons, 2011.